6

Shrinkage defects: Free surface deformation during solidification of Metal Alloys

6.1 INTRODUCTION

This final chapter is attributed to the model development to predict shrinkage defect in the form of free surface deformation during binary alloy solidification. The effect of shrinkage flow on the free surface deformation is accounted for by using the volume of fluid method during alloy solidification process. The existing models reported in literature reveals a strong dependence of the shape of shrinkage-defects on the heat removal rate. None of these existing predictions involve enthalpy updating scheme to evaluate solid and liquid volume fractions. The present study focuses on modifying the enthalpy updating scheme in it's existing framework to include tracking of the evolving free surface caused by shrinkage induced flow. The results of the numerical model is validated with the existing analytical models and is further compared with the numerical and experimental results reported by Sun and Garimella [2007]. The study is focused on predicting the macro-scale shrinkage defect during eutectic and alloy solidification process in 2-D mold cavity.

For the numerical investigation presented in this chapter, analysis pertaining to the prediction of free surface deformation and macro-segregation is performed for two different cavity geometries. The first geometry for the study consists of a rectangular mold cavity with a riser at the center (figure 6.1(a)) , and is analogous to the one detailed in Chiang and Tsai [1992b]. The second geometry once again consists of a rectangular mold cavity, but the top surface of the cavity is considered to be completely open (figure 6.1(b)). The analysis involves two distinct case studies. The first set of case study is associated with the free surface tracking during the solidification of pure Aluminium. The second set of case study involves prediction free surface evolution and macro-segregation during the solidification of Al-4.1 wt.% Cu alloy. The cavity is initially filled with molten metal at a temperature: (i) greater than its melting temperature ($T_i > T_m$) for the case study associated with solidification of pure Aluminium, and (ii) greater than the liquidus temperature corresponding to the nominal composition ($T_i > T_L$) for the case study involving solidification of Al-4.1 wt.% Cu alloy. Solidification is ensued by maintaining the mould wall temperatures below the freezing point temperature (T_m) and eutectic temperature (T_e) for pure Aluminium and Al-4.1 wt.% Cu alloy respectively. During the analysis, the free surface is considered to be adiabatic.

6.2 MATHEMATICAL MODELLING

The requirement of free surface tracking due to the shrinkage effect renders the solidification model to address a solidification domain consisting of all three phases, namely solid, liquid, and gas (or void). However, the gas phase consisting of air or other dissolved gases in the melt has a negligible density as compared to the solid and liquid phases. Therefore, the terms appearing in mass and momentum equations involving gas (or void) phase densities are neglected to obtain a simplified model. The price we pay for this simplification is reflected by the inability to obtain interface orientation at individual control volumes when the reconstruction algorithm is implemented to track the free surface. Particularly, for course grid resolution, the model provides

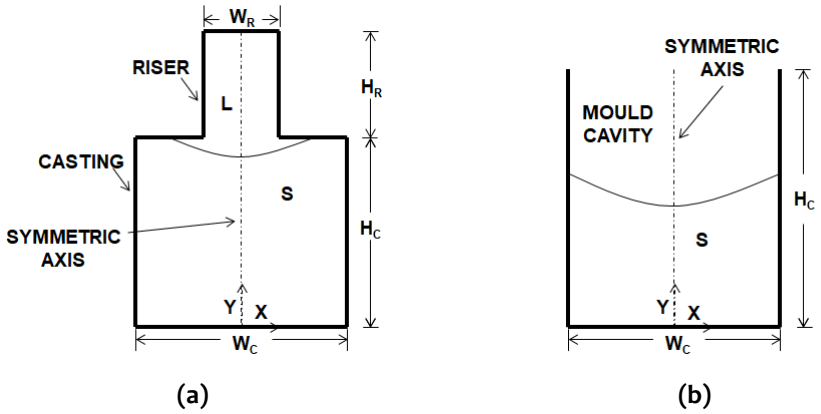

Figure 6.1 : Schematic of the physical domain of interest during the (a) riser-cavity and (b) mold cavity analysis

a free surface with steps rather than a smooth one. Even with fairly high grid resolution, such a broken representation of free-surface can not be avoided completely. This simplification renders one of the major limitations of the solidification model proposed in this chapter.

The continuum equation for mass, momentum and species are already discussed in previous chapter (Eq. 5.1-5.3 and 5.5). Coming to energy conservation, it is derived as proposed by Bennon and Incropera [1987a] and is expressed in terms of temperature. While formulating, all the three phases co-exist, i.e., solid, liquid, and void phase system. The mass averaged enthalpy is defined as: $h = f_s h_s + f_l h_l + f_v h_v$, $h_s = c_{ps}T$, $h_l = (c_{ps} - c_{pl})T_e + h_{sl} + c_{pl}T$, and $h_v = c_{pv}T$; where $c_{p\phi}$ is specific heat of the individual phase ϕ, and T_e is eutectic temperature. Once again, the void density being negligibly small, the terms associated with void enthalpy can be conveniently neglected. Also, the thermal conductivity of the gas being negligibly small as compared to solid or liquid metals and metal alloys can be neglected for case studies under consideration. A detailed derivation of the energy conservation equation is presented in Appendix A. Considering the above assumptions the energy equation is obtained as follows:

Energy

$$\frac{\partial}{\partial t}(\rho T) + \nabla.(\rho \mathbf{V} T) = \nabla.\left(\frac{k}{c_{ps}}\nabla T\right) - \nabla.\left[\left(\frac{c_{pl}}{c_{ps}} - 1\right)\rho \mathbf{V} T\right] - \frac{\partial}{\partial t}\left(\frac{\rho_s g_l h_{sl}}{c_{ps}}\right) - \frac{\partial}{\partial t}\left[g_l\left(\frac{c_{pl}}{c_{ps}} - 1\right)(\rho_l T - \rho_s T_e)\right] - \left(\frac{\rho_s h_{sl}}{c_{ps}} - \rho_s T_e\left(\frac{c_{pl}}{c_{ps}} - 1\right)\right)\frac{\partial}{\partial t}(g_v) \quad (6.1)$$

As we can see from Eq.6.1, void volume fraction (g_v) turns out in one of the four source terms in the energy equation, which is significantly different from the energy equation used in the previous two chapters. The solutal buoyancy term appearing in Eq.5.3 and species equation (Eq.5.5) can be removed completely from the numerical framework while solving for pure metal.

Free surfaces are distinguished by discontinuities in one or more variables. For the present study, the void-fluid interface is considered a free surface. This free surface movement is captured and embedded in a fixed grid finite volume framework by implementing the VOF (volume of fluid) method [Hirt and Nichols, 1981]. The volume fraction of the void phase g_v is the characteristic function and is advected passively within the fluid flow. The value of g_v varies from 0, for a grid cell filled with fluid, to 1, for completely void grid cells, and at the free boundary, the value lies

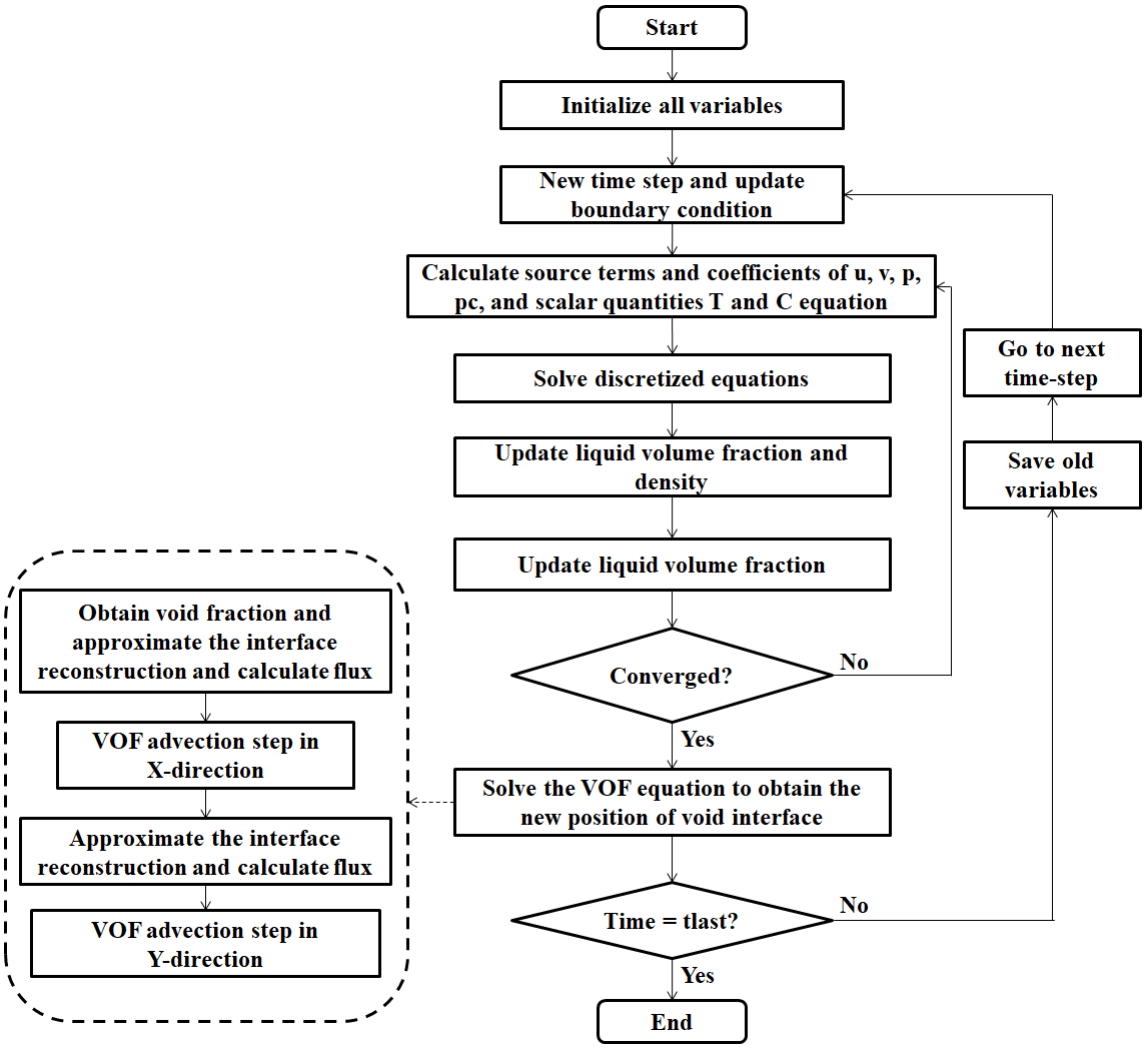

Figure 6.2 : Flowchart for the numerical algorithm

between 0 to 1. The evolution of VOF function g_v captures the evolution of the free surface and satisfies the following advection equation [Hirt and Nichols, 1981].

Advection

$$\frac{\partial}{\partial t}(g_v) + \nabla.(g_v \mathbf{V}) - g_v(\nabla.\mathbf{V}) = 0 \tag{6.2}$$

In order to save computational time, the simulation for all the cases are performed considering symmetry about the central y-axis. At free surface gauge pressure p is assumed to be zero. All the surfaces for the case study involving the cavity with riser are perfectly insulated except the bottom wall. On the other hand, for the case study considering a mold cavity with an open top, all the surfaces of the cavity are exposed to cold temperature conditions. The governing equations for u and v momentum, along with other scalar quantities, are discretized using the finite volume method to obtain a system of linear algebraic equations that are solved in an iterative manner for each time step [Patankar, 2018; Versteeg and Malalasekera, 2007]. Coefficients involving convection and diffusion are computed using a power-law scheme. Initially, the flow field is obtained by solving momentum and continuity equations using the SIMPLER algorithm, and later other scalar quantities like temperature and species are determined at each iteration step. The solid-liquid interface movement during the phase change is tracked using a similar volume fraction updating scheme, as discussed earlier in Eq.5.8.

The advection equation (Eq. 6.2) for the void fraction is discretized by using a standard conservative finite-difference algorithm based on fractional step or operator split method. The solution method involves the splitting of Eq. 6.2 in each sweep direction. In order to conserve the void fraction and to gain second-order accuracy, it is necessary to discretise g_v implicitly in one sweep direction and explicitly in other [Puckett et al., 1997]. The interface reconstruction requires the estimation of void fraction fluxes at the faces of control volumes. A donor-acceptor scheme is used for calculating these fluxes. Estimation of these fluxes depends on the mean surface orientation, which is convected either normal or parallel to itselfHirt and Nichols [1981]. For the present study, the surface is mostly convected normal to itself as there is no perturbation in a parallel direction. The details of the void fraction (g_v) calculation is provided in Appendix C. The entire solution algorithm incorporating the VOF scheme is shown in the flow chart provided in figure 6.2.

6.3 RESULT AND DISCUSSION

6.3.1 Validation

The numerical model proposed in this chapter is first validated with the existing simulation and experimental results reported by Sun and Garimella [2007]. Sun and Garimella [2007] studied the solidification surface deformation due to shrinkage effect during the casting of trinitrotoluene (TNT) in a cylindrical cavity. TNT has a high-density ratio (ρ_s/ρ_l), and surface deformation due to shrinkage is prominent during the experiments involving the solidification of TNT. The experiment reported by [Gudibande and Iyer, 2016] involves solidification of TNT in a cylindrical mold of diameter 39 *mm* and aspect ratio (height to diameter) 5.65. TNT was initially at a temperature slightly higher than its melting point and was allowed to solidify by controlling the temperatures of the side and bottom walls using steam heaters. For the present simulation, the temperatures measured on the side and bottom walls were used as a boundary condition and is shown in figure 6 of Sun and Garimella [2007]. The figure 6.3(a) shows the comparison of present numerical results with the results reported by Sun and Garimella [2007]. Although the numerical results showed a better agreement, there was an inconsistency between numerical and experimental results. This can be attributed to the presence of dissolved gases causing nucleation of voids during

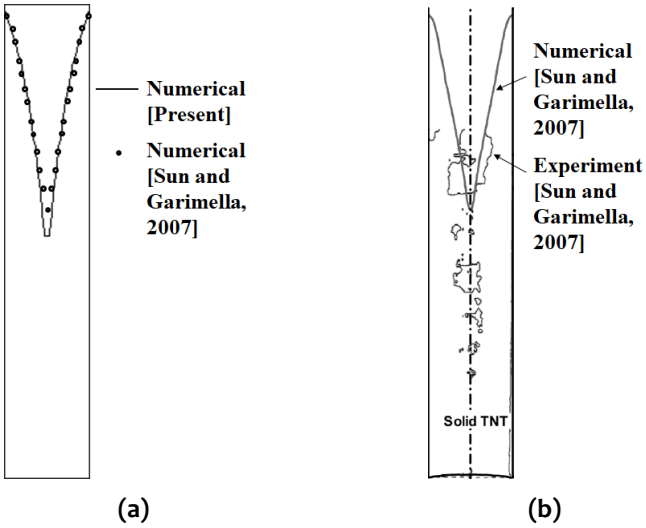

Figure 6.3 : Comparison between (a) the numerical results from the proposed model and the numerical results reported by Sun and Garimella [2007] and (b) numerical and experimental results reported by Sun and Garimella [2007].

solidification [Sun and Garimella, 2007].

Once confidence is built, the numerical investigation is extended for three different case studies viz. (a) solidification of pure aluminium in a rectangular mold with riser (properties of pure aluminium is provided in Table 4.1), (b) solidification of pure aluminium in a rectangular mold cavity with an open top, and (c) solidification of pure Al-4.1 wt.% Cu alloy in a rectangular mold cavity with an open top (properties of Al-4.1 wt.% Cu alloy is provided in Table 5.1). The present analysis are performed to understand the nature of free surface deformation and macro-segregation as a consequence of applied boundary temperature and the mold cavity shape.

6.3.2 Solidification of pure aluminium in a rectangular mould with riser

For this particular numerical analysis, the dimensions of the cavity ($H_C \times W_C$) and riser ($H_R \times W_R$) are considered to be $150 \times 200\ mm^2$ and $100 \times 50\ mm^2$ respectively. The simulation is carried out for one of the symmetric halves. Uniform grid cells of 72×48 in the casting section and 48×12 in the riser section is used. The analysis is conducted using the properties of pure Al, as specified in Table 4.1. The domain is initially filled with liquid metal up to a height of $\approx 246\ mm$ from the bottom and is maintained at a temperature of $1033\ K$. The cooling is ensued by decreasing the temperature of the bottom wall below the melting point. Two different cooling temperatures viz. $300\ K$ and $500\ K$ are selected for the analysis. The results pertaining to convection currents and free surface evolution due to density difference are presented in figures 6.4 and 6.5 at different time instants for two different cold bottom temperature values. At the initial stage of solidification, the interface growth rate is high. Strong convection current induced by this fast growth rate of solid front causes the shrinkage induced flow to penetrate deeper into the melt region inside the cavity. As a result, two counter-rotating convection roll forms having a net downward flow along the central line of the mold cavity (figures 6.4(a) and 6.5(a)). The solid front growth and shrinkage induced flow is accompanied by a continuous lowering of the free surface in the riser section. However, with the progression of the solidification process, the growth rate of the solid front diminishes with time. As a result, the intensity of shrinkage induced flow also diminishes

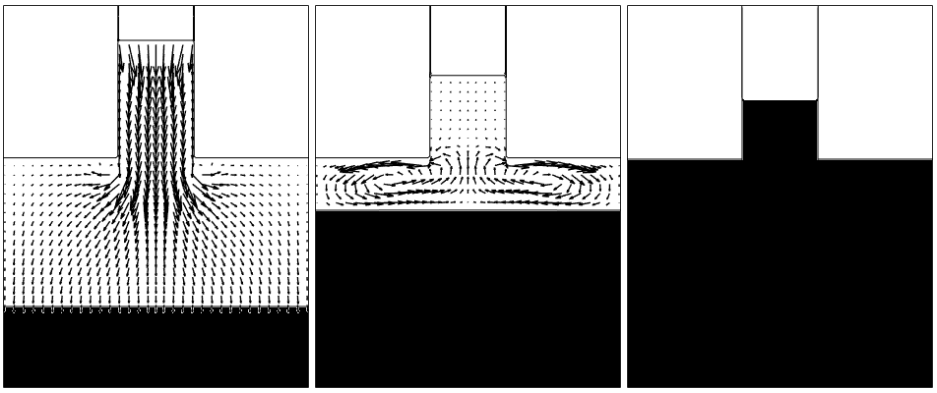

(a) (b) (c)

Figure 6.4 : Flow field, solid front, and free surface evolution at time instants (a) 20 s (b) 100 s and (c) 230 s for T_b=300 K.

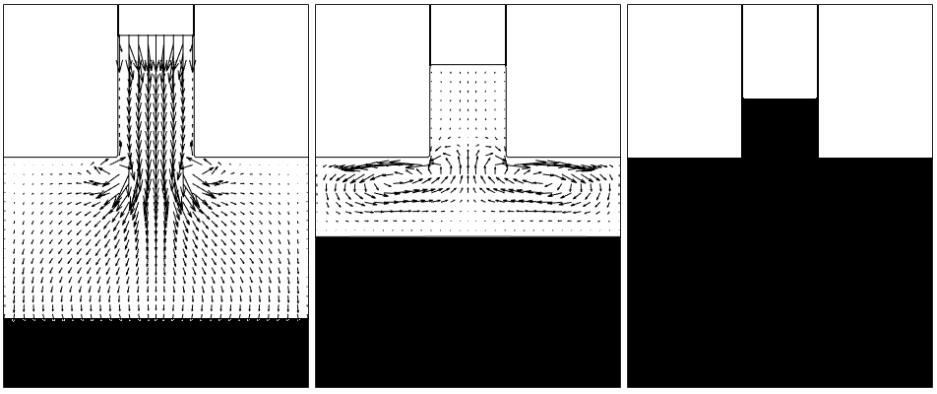

(a) (b) (c)

Figure 6.5 : Flow field, solid front, and free surface evolution at time instants (a) 20 s (b) 100 s and (c) 310 s for T_b=500 K.

with time, eventually manifesting flow reversal phenomena discussed in the third chapter. The flow reversal phenomena is characterized by the existence of two counter-rotating convection roll with a net upward flow along the central line of the mold cavity (figures 6.4(b) and 6.5(b)). The complete solidification is attained at 230 s and 310 s for cold boundary temperatures 300 K and 500 K respectively (figure 6.4(c) and 6.5(c)). Although the free surface is successfully traced, the final cast product is devoid of any free surface deformation due to insulated boundary conditions at the side walls. The next case study involving the cooling of the entire mold cavity wall is performed towards the prediction of free surface deformation due to shrinkage.

6.3.3 Solidification of pure aluminium in a rectangular mould cavity with open top

For the open mold cavity investigation, the riser part is dropped, causing the entire top surface of the cavity to be open to the atmosphere. The cavity height and width of the casting domain is considered to be 250 mm and 200 mm, respectively. The simulation is once again carried

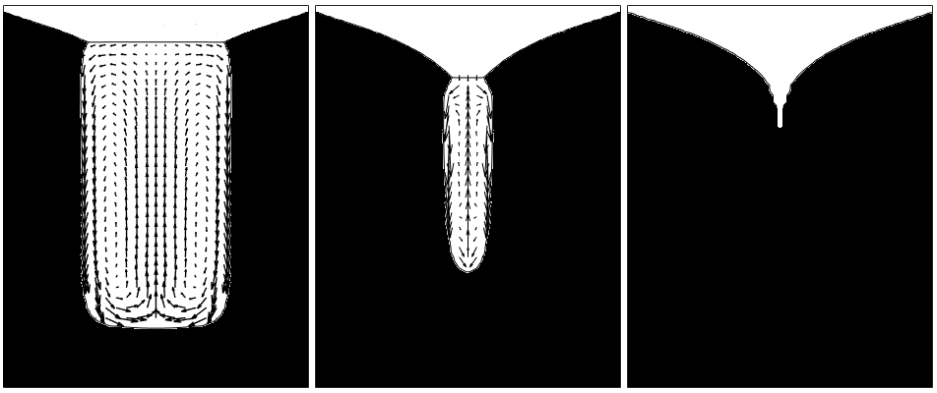

Figure 6.6 : Flow field, solid front, and free surface evolution at time instants (a) 10 s (b) 25 s and (c) 35 s for T_c=300K.

out for one of the symmetric halves with a uniform grid resolution of 100×40. Cooling ensues from the bottom and side walls by maintaining the temperature to 300 K. The free surface is treated to be adiabatic. Figure 6.6 shows the estimated numerical results concerning the evolution of free surface, velocity field and solid front growth at times 10 s, 25 s, and 35 s.

As is evident, the solid front grows from all cold surfaces into the mold cavity. However, the suction created by the shrinkage effect causes a funneling effect at the upper section of the cavity, and the solid front follows this funnel shape. As solidification propagates further, a considerable amount of the melt at the core contracts continuously, and the funnel shape of the free surface becomes more and more prominent. At the completion of the solidification, the disfigured final surface of the casting resembles a V-shaped cavity. This V-shaped cavity is characterized by a wide mouth covering the entire opening of the mold cavity and a steep tapering at the bottom end. The nature of the open surface deformation is essentially regulated by the aspect ration of the cavity and the cooling condition implemented at the walls of the mold. The next two subsections discuss these two attributes.

Effect of varying aspect ratio of the mould cavity

During a casting process, together with the heat transfer boundary conditions, the geometry also plays an important role in the formation of shrinkage cavities. To study the influence of geometry, a set of three simulations are performed for the solidification of aluminium in rectangular cavities with varying aspect ration. The aspect ration of the mold cavity is varied by changing its width, while the height is kept constant. The width for the three different cavities are chosen as 200 mm, 140 mm, and 80 mm, while the height is considered to be 250 mm for all three cases. The number of grids for symmetric halves are chosen to be 40, 28, and 16, respectively, in the direction of width. Along the direction of height, the grid resolution is considered to be 100. The molds are initially filled with molten aluminium to a height of $\approx$ 245.6 mm. The 2-D cavities are cooled from all three sides while the top surface is kept open. The heat extraction rate of 2×10^6 W/m^2 is applied at the side walls, whereas 10^5 W/m^2 is applied at the bottom wall [Bhattacharya, 2014]. Figure 6.7 shows the shape of the castings after complete solidification.

As is evident from figure 6.7, the qualitative resemblance prevails for all three aspect ration under consideration. However, the penetration depth of the surface deformation decreases with the decreasing width of the cavity. From the case study presented here, the maximum depth of

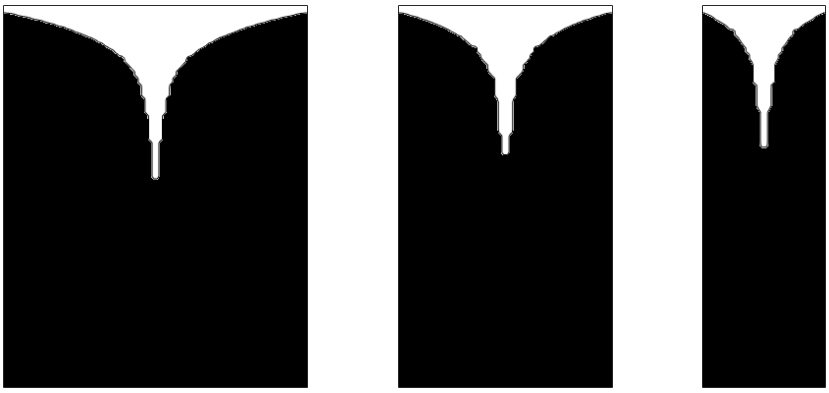

Figure 6.7 : Comparison of the free surface deformation in the final cast products for varying cavity width (W_C) (a) 200 *mm*; (b) 140 *mm*; (c) 80 *mm*. For all three cases the heat extraction rates from side walls and bottom wall are $q_s^{"} = -2 \times 10^6\ W/m^2$ and $q_b^{"} = -10^5\ W/m^2$ respectively

deformation is found to be 122.1076 *mm* from the bottom for 200 *mm* cavity width. Since smaller width corresponds to a significantly larger heat removal rate from side walls as compared to the cold bottom wall, the solid front propagating from the side walls get fused more rapidly, leading to the reduced depth of free surface deformation. Significant material losses may be incurred during the development of a finished product from this type of casting.

Effect of heat extraction rate at the boundary of the mould cavity

For this set of case study, numerical simulations are performed by varying the heat extraction rate at the boundaries. And the effect of varying heat extraction rate on the free surface deformation is studied. For this analysis, cavity height and width are chosen to be 250 *mm* and 200 *mm* respectively. Grid resolution of 100×42 is considered for the symmetric half. Heat is removed from the side walls at a constant rate of $2 \times 10^6\ W/m^2$. The initial temperature is chosen to be 943 K. Four different simulations are performed with bottom wall being subjected to a heat flux of $4 \times 10^6\ W/m^2$, $2 \times 10^6\ W/m^2$, $1 \times 10^6\ W/m^2$ and $0.1 \times 10^6\ W/m^2$ respectively. Figure 6.8 shows the comparison of the final deformed surfaces of the cast products for four different heat extraction rates from the bottom surface. The depth of the funnel-shaped free surface deformation is found to be deeper for lower cooling rates at the bottom surface (figure 6.8(a)-(d)). When the cooling rate at the side walls is lower as compared to the bottom wall, the growth rate of the solid front from the side walls are comparatively lower at the upper portion of the cavity. However, the combined effect of a higher heat removal rate from the bottom wall and heat removal from side walls favor a faster solidification rate at the lower portion of the cavity. The combination of these two effects are manifested by a funnel-shaped cavity with a wider and shallower fissure end at the bottom. On the other hand, a decrease in heat removal rate from the bottom surface favors a faster front growth rate from the side walls leading to once again a funnel-shaped cavity but with a narrower and deeper fissure end at the bottom. However, the results obtained in the previous and present subsections are not very conclusive other than stating the robustness of the proposed model. Further study is required with much more wider variation in aspect ratio and cooling rates to obtain a more generalised theory relating the depth of shrinkage deformation with these two parameters. This parametric study is beyond the scope of the present thesis and is left as future scope of the present study. This particular type of shrinkage cavity predicted by the proposed model is known as pipe shrinkage, and such defects lead to significant loss of material during

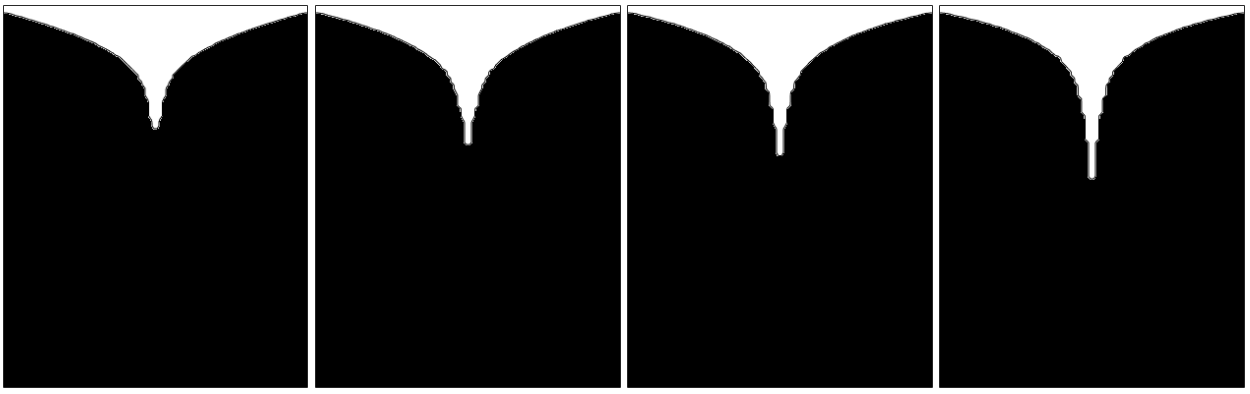

Figure 6.8 : Comparison of the free surface deformation in the final cast products for same side wall heat flux of $-2 \times 10^6\ W/m^2$ and different bottom wall heat fluxes (a) $-4 \times 10^6\ W/m^2$; (b) $-2 \times 10^6\ W/m^2$; (c) $-1 \times 10^6\ W/m^2$; and (d) $-0.1 \times 10^6\ W/m^2$.

machining to obtain the finished product. Also, the presence of sharp corners may lead to stress concentrations around those areas and consequently reduce the strength of the casting.

6.3.4 Solidification of pure Al-4.1 wt.% Cu alloy in a rectangular mould cavity with open top

In this concluding subsection, the implementation of the proposed model is extended to predict free surface deformation and macro-segregation evolution during binary alloy solidification. Solidification of the Al-4.1 wt.% Cu alloy system in a 2-D top open square mold cavity of $100 \times 100\ mm^2$ is analysed. Once again, the analysis is carried out for one of the symmetric halves with a uniform grid resolution of 100×50 along with height and width directions, respectively. The temperature of the liquid melt is initially maintained at 930 K. The heat is extracted by applying a constant temperature boundary condition ($T_c = 800\ K$) for all side walls, and heat removal by means of convective heat transfer is applied at the bottom surface. An effective heat transfer coefficient of $2000\ W/m^2K$ is assigned between the bottom wall and chiller maintained at 293 K. The reason for assigning such a high value of the effective heat transfer coefficient is simply to promote a faster cooling rate for achieving a rapid growth rate of the solid front in the proposed numerical framework. The properties of the alloy system are provided in Table 5.1.

Figure 6.9 (a)-(c) describe the flow field, free surface, and macro-segregation ($(C - C_0)/C_0$) at different time instants of the solidification process under the applied initial and boundary conditions. The thermal and solutal buoyancy effects aid each other for this particular alloy system due to heavier solute (Cu) rejection in the melt during the solidification process. As a result, the flow field in the pure melt and mushy region is quite similar to the flow field obtained during a similar case study involving pure aluminium in the previous subsection. Once again, the free surface gradually evolves into a funnel-shaped depression similar to the previous case study. After the completion of the solidification process concentration C is found to vary within the range of 3.16 to 4.6935 wt.% Cu. The final macro-segregation is characterized by a hollow truncated cone of negative segregation ($C < C_0$) at the bottom half of the core surrounded by regions of positive segregation ($C > C_0$). A patch of large positive segregation is complementing the core negative segregation zone just above the core and culminates into a very high solute concentration adjacent to the fissure end of the funnel shaped free surface. It is pertinent to mention here that the region adjacent to the bottom-most end of the free surface solidifies at the end stage of the solidification process. Therefore the melt remaining at the final stage of the solidification process contains a large amount of rejected solute resulting in significantly large positive segregation in the domain undergoing the liquid-solid phase transition at the final stage of the solidification

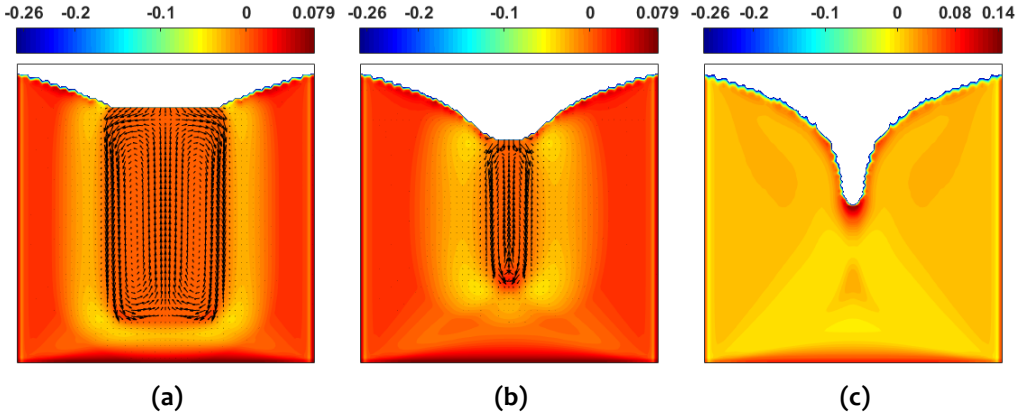

Figure 6.9 : Flow field, free surface and macro-segregation ($(C - C_0)/C_0$) evolution at time instants (a) 10 s, (b) 20 s (c) after completion of the solidification process

process. Reports concerning the experimental and numerical observation of such hollow cone of negative segregation [Wang et al., 2005; Ahmadein et al., 2015; Ge et al., 2017] convey the validity of the proposed model qualitatively. The large positive segregation adjacent to the fissure end of the free surface predicted by the proposed model is also physically consistent. Therefore the proposed model has the viability the predict physically consistent results. The implementation of the proposed model will be highly beneficial for the prediction of shrinkage induced casting defects.

6.4 SUMMARY

In this chapter, a numerical model is developed and proposed to capture the free surface deformation due to shrinkage during the solidification of pure substances and binary alloys. The basic framework of the enthalpy-porosity scheme is modified and coupled with the VOF (volume of fluid) scheme to estimate the void fraction. The interface reconstruction is approximated using the donor-acceptor scheme to estimate the flux of volume across the faces. The proposed model is validated by comparing the results obtained from the proposed model with reported observations concerning free surface deformation during the solidification of TNT. Reasonably good agreement between the results obtained from the proposed model and reported data is obtained. After validation, three different case studies are performed using the proposed model, namely: (i) solidification of pure aluminium in a bottom cooled mold cavity with a riser at the center, (ii) Solidification of pure aluminium in a top open mold cavity with all cavity surfaces being subjected to Dirichlet or Neumann boundary conditions respectively, and (iii) Solidification of pure Al-4.1 wt.% Cu alloy in a top open mold cavity with side and bottom walls being subjected to Dirichlet and mixed boundary conditions, respectively. The analysis involving the first case study successfully captured the shrinkage induced flow field and the gradual lowering of the planner free surface inside the riser. The analysis involving the second case study successfully captured the free surface deformation resembling a funnel shape with an elongated fissure end at the bottom. The analysis pertaining to the second case study also indicated the dependence of free surface deformation depth on the aspect ratio of the mold cavity and heat removal rate. The analysis involving the third case study once more demonstrated the robustness of the proposed model by successfully capturing physically consistent free surface deformation and macro-segregation pattern.

...